European Journal of Pharmaceutics and Biopharmaceutics 202 (2024) 114414

Contents lists available at ScienceDirect

European Journal of Pharmaceutics and Biopharmaceutics

journal homepage: www.elsevier.com/locate/ejpb

Unraveling mRNA delivery bottlenecks of ineffective delivery vectors by co-transfection with effective carriers

Rik Oude Egberink [a], Deni M. van Schie [a], Ben Joosten [a], Lisa.T.A. de Muynck [a], Ward Jacobs [a], Jenny van Oostrum [a], Roland Brock [a,b,*]

[a] Department of Medical BioSciences, Research Institute for Medical Innovation, Radboud University Medical Center, 6525 GA Nijmegen, the Netherlands
[b] Department of Medical Biochemistry, College of Medicine and Medical Sciences, Arabian Gulf University, Manama 329, Bahrain

ARTICLE INFO

Keywords:
Co-transfection
Endosomal escape
Gene therapy
mRNA delivery
Nanomedicine
Nanoparticles

ABSTRACT

The messenger RNA (mRNA) SARS-CoV-2 vaccines have demonstrated the therapeutic potential of this novel drug modality. Protein expression is the consequence of a multistep delivery process that relies on proper packaging into nanoparticle carriers to protect the mRNA against degradation enabling effective cellular uptake and endosomal release, and liberating the mRNA in the cytosol. Bottlenecks along this route remain challenging to pinpoint. Although methods to assess endosomal escape of carriers have been developed, versatile strategies to identify bottlenecks along the delivery trajectory are missing. Here, it is shown that co-incubating an inefficient nanoparticle formulation with an efficient one solves this problem. Cells were co-incubated with mRNA nanoparticles formed with either the efficient cell-penetrating peptide (CPP) PepFect14 or the inefficient CPP nonaarginine (R9). Co-transfection enhanced cellular uptake and endosomal escape of R9-formulated mRNA, resulting in protein expression, demonstrating that both vectors enter cells along the same route. In addition, cells were transfected with a galectin-9-mCherry fusion protein to detect endosomal rupture. Remarkably, despite endosomal release, mRNA remained confined to punctate structures, identifying mRNA liberation as a further bottleneck. In summary, co-transfection offers a rapid means to identify bottlenecks in cytosolic mRNA delivery, supporting the rational design and optimization of intracellular mRNA delivery systems.

1. Introduction

With the SARS-CoV-2 pandemic just behind us, the therapeutic value of the capacity of messenger RNA (mRNA) to elicit cellular protein expression has been firmly established. Proper packaging in delivery vehicles is crucial to apply mRNA therapeutically, which protects the mRNA from degradation and induces efficient cellular uptake and endosomal release [1,2]. Packaging of mRNA is achieved through (electrostatic) complexation with cationic lipid- or peptide-based carriers. So far, lipid-based carriers, particularly lipid nanoparticles (LNPs), have seen the most widespread clinical implementation. However, LNPs suffer from a number of shortcomings such as limited stability [3,4], the multi-component lipid composition, the need for microfluidic devices for manufacturing, and non-natural degradation products of lipid components. Moreover, current LNP formulations have been shown to induce inflammatory responses [5] and also upon local intramuscular administration, there is considerable leakage into systemic circulation with sequestration by the liver [6]. Finally, the ionizable lipid component may react with and thereby inactivate the mRNA [7]. Thus, there is still an urgent need for alternative formulations with less components, easier manufacturing, higher control of delivery route and less concerns of side reactions. Cationic peptides and other peptide and polymer-based materials are being broadly explored as potential carriers [8–11]. However, so far, only a few show activity, and for a specific formulation, it is a challenge to pin down the relevant bottlenecks of the delivery process [12].

Cytosolic delivery of mRNA nano-formulations is a multi-step process. In circulation, nanoparticles (NPs) rapidly acquire a protein corona, and this process must not disrupt the RNA formulation. Furthermore, the mRNA must be protected from nucleases inside and outside the cell and formulations that succeed in plasmid DNA delivery can still fail in the protection of mRNA [13,14]. Following interaction

* Corresponding author at: Dept. of Medical BioSciences, Radboud University Medical Center, Geert Grooteplein 28, 6525 GA Nijmegen, the Netherlands.
E-mail addresses: rik.oudeegberink@radboudumc.nl (R. Oude Egberink), deni.vanschie@ru.nl (D.M. van Schie), ben.joosten@radboudumc.nl (B. Joosten), lisa.demuynck@ru.nl (Lisa.T.A. de Muynck), ward.jacobs@radboudumc.nl (W. Jacobs), jenny.vanoostrum@radboudumc.nl (J. van Oostrum), roland.brock@radboudumc.nl (R. Brock).

https://doi.org/10.1016/j.ejpb.2024.114414
Received 25 May 2024; Received in revised form 10 July 2024; Accepted 12 July 2024
Available online 14 July 2024

with cells, uptake must be induced. Most mRNA-containing nanoparticles are taken up by cells via endocytosis [15]. Endosomal release is the rate-limiting step in mRNA delivery [16,17]. Importantly, it is paramount for therapeutic efficacy that endosomal escape occurs before the fusion of endosomes with lysosomes to form degradative endolysosomes [18]. Quantitative *in vivo* studies have revealed that endosomal escape efficiencies range from ~ 0.3 % to 1–2 % for siRNA and antisense oligonucleotides, respectively [19,20]. Moreover, for small interfering RNAs (siRNA), as much as 70 % of the internalized RNA leaves the cells through exocytosis before escaping the endosomes [21]. Moreover, endosomal escape alone is insufficient for mRNA expression since once inside the cytosol, mRNA must be released from the carrier before it can be translated into protein even though the details on how this occurs have hardly been addressed. Observations for LNPs suggest that unpacking is driven by endosomal acidification and may thus be part of the endosomal release process [17].

Studies indicate that even for efficient delivery vehicles, well over 95 % of the RNA dose does not contribute to the therapeutic effect. As the toxicity of RNA therapeutics is primarily due to the membrane-destabilizing characteristics of the cationic carrier [22–26], these inefficiencies compromise the therapeutic application of mRNAs. Moreover, recent studies have shown that for LNPs, as much as 40–80 % of the nanoparticles do not contain any mRNA [27,28]. Thus, there is a real opportunity to simultaneously reduce the toxicity and costs of mRNA therapeutics by optimizing the individual steps along the uptake pathway for alternative types of delivery vehicles.

Several strategies have been presented to detect the endosomal escape capabilities of nanosized carriers, among which are protein complementation assays. In these assays, a protein is split into two fragments. Once these fragments are in spatial proximity, they will interact and form the complete, functional protein [29]. These proteins typically are reporter proteins for which robust read-outs exist. The first of these to be employed in studies on endosomal release relied on the delivery of the 11th β-strand of GFP into cells that (constitutively) express the non-fluorescent GFP1-10 [30,31]. More sensitive by four orders of magnitude are split luciferase approaches [32–34]. Alternatively, a Renilla luciferase zymogen that is only activated once in the cytosol was co-formulated with the mRNA [35]. To detect endosomal rupture, fluorescent fusion proteins of galectins can be expressed in the cytosol. Galectins are a family of ß-galactoside-binding lectins. Without endosomal disruption, galectins are homogeneously distributed throughout the cytosol [36]. However, when membrane damage exposes the ß-galactosides of the inner leaflet of the endosomal membrane to the cytosol, galectins are recruited to the endosome and bind the exposed glycans, leading to a punctate distribution of fluorescence [37,38].

Whereas the strategies summarized above help discriminate delivery vehicles with efficient from those with inefficient endosomal release, they fall short in instructing about the specific shortcomings of a carrier along the whole delivery trajectory. A platform that fails to induce endosomal release may still effectively liberate mRNA once inside the cytosol. The availability of such strategies is essential for a rational design and optimization of delivery vehicles. Here, we demonstrate the co-incubation of delivery vectors as a solution to this problem. On the one hand, we combined mRNA NPs formed with the inefficient cell-penetrating peptide (CPP) R9 with mRNA NPs formed with the efficient CPP PepFect14 (PF14). Using fluorescently labeled mRNA, these co-transfections revealed that PF14 mRNA NPs enhanced the cellular uptake of R9-formulated mRNA, highlighting that both types of nanoparticles enter via the same route but strongly differ in their capacity to induce endocytosis. Also, the results show that degradation of mRNA in R9 nanoparticles is not the reason for their poor performance.

Moreover, expression of R9 NP-delivered mRNA was observed only in the presence of PF14-mRNA NPs, identifying the lack of endosomal release as a further shortcoming of R9-mRNA NPs. By comparison, co-incubation of R9 with a lipid-based mRNA carrier, not showing endosomal entrapment of mRNA, did not yield an mRNA delivery benefit. Most experiments were conducted in the murine pre-osteoblast MC3T3 cells. We employed this cell line as it has a spread out morphology and is thus highly suited for microscopy studies of particle uptake [39]. However, the key concept was also validated in HeLa cervical carcinoma cells, which is a widely employed cell model for delivery studies, C5120 human primary fibroblasts [40] and bone marrow-derived mesenchymal stem cells as a further primary cell line [41].

Visualizing galectin-9 in co-transfections revealed that although PF14 efficiently mediated endosomal disruption, mRNA was only poorly dissociated from NPs, identifying a crucial bottleneck for this peptide. Lastly, we used super-resolution microscopy to rule out that mRNA delivery benefits of co-transfections were not simply due to mRNA exchange between PF14 and R9 NPs.

2. Materials and methods

2.1. Cell culture

Subconfluent cultures of the HeLa human cervical adenocarcinoma cell line (DSMZ no. ACC57, Leibniz Institute DSMZ-German Collection of Microorganisms and Cell Cultures, Braunschweig, Germany) were maintained in RPMI 1640 Medium (Dutch modification, Gibco, Waltham, MA, USA, Cat. No. 22409031) supplemented with fetal bovine serum (FBS; Gibco, Cat. No. 10270-106), and GlutaMAX (Thermo Fisher Scientific, Waltham, MA, USA, Cat. No. 35050038). All experiments were performed with HeLa cells with a passage number lower than 15.

Subconfluent cultures of the MC3T3-E1 subclone 4 (CRL-2593, American Type Culture Collection; ATCC, Manassas, VA, USA) pre-osteoblastic murine cell line were maintained in Minimal Essential Medium α (α-MEM; Gibco, Cat. No. A10490-01), supplemented with 10 % v/v FBS. All experiments were performed with MC3T3 cells with a passage number lower than 25. hBMSCs were isolated from iliac bone fragments from healthy donors after surgery (Department of Maxillofacial Surgery, Radboudumc, The Netherlands) after ethical approval (Commissie Mensgebonden Onderzoek: dossier number #2017-3252) as described previously [41]. In line with the criteria as set by the International Society for Cellular Therapy (ISCT) [42], hBMSCs immunophenotypically demonstrated to express characteristic MSC markers (>95 % immunopositive for CD73, CD90 and CD105, and immunonegative for CD45) and the capacity to undergo osteogenic differentiation. hBMSCs were maintained in complete α-MEM and were only used from passages 2-7.

Subconfluent cultures of the C5120 skin fibroblasts were maintained in Medium 199 supplemented with 10 % v/v FBS and GlutaMAX [40]. All experiments were performed with C5120 cells with a passage number lower than 15. All experiments were performed with MC3T3 cells unless stated otherwise.

2.2. Messenger RNA (mRNA)

CleanCap enhanced green fluorescent protein (eGFP) mRNA (L-7601) and 5-methoxyuridine-substituted mCherry mRNA (L-7203) were purchased from Trilink Biotechnologies (San Diego, CA, USA). Secreted nanoluciferase (Luc), mCherry, eGFP, and mRNA labeled with Alexa Fluor (AF), AF488, AF568, and AF647 were all purchased from RIBOPRO (Oss, The Netherlands). In the mRNAs about 25 % of UTPs were fluorescently labeled which translates into about 20–35 labels per mRNA molecule or less than 1 in 20 nucleotides. All mRNA was aliquoted at 100 ng μL^{-1} in nuclease-free water (Thermo Fisher Scientific, Waltham, MA, USA, Cat No. AM9937) in DNA LoBind tubes (Eppendorf, Hamburg, Germany), snap-frozen in liquid nitrogen and stored at −80 °C until use. Before use, the mRNA solutions were thawed and kept on ice.

2.3. mRNA nanoparticle formation

Peptide-mRNA polyplexes were formulated as previously described [43,44]. In short, two separate stock solutions of mRNA and peptide were prepared in MQ and simultaneously aspirated with electronically dispensing pipettes (E4 Electronic Pipette, LTS E4-100XLS+, Mettler-Toledo Rainin, LLC, Oakland, CA, USA) at a flow rate of 11 mL min^{-1}. All polyplexes were formed at a concentration at least tenfold the final intended concentration for transfections. The final concentration for PF14 mRNA NPs was 2 μM unless stated otherwise. For R9 mRNA NPs, we made particles with a final concentration of 1.11 μM R9 (referred to as 1 μM), which contained an equivalent mRNA dose to 2 μM PF14. Moreover, we also tested R9 mRNA NPs at 5.16 μM (referred to as 5 μM), which is 4.6 times more mRNA compared to 2 μM PF14.

For the formation of cationic lipid-based complexes (lipoplexes), Lipofectamine MessengerMAX (LMM; Thermo Fisher Scientific, Waltham, MA, USA) was used according to the manufacturer's instructions. In short, LMM was incubated in Opti-MEM (Gibco, Cat. No. 11058021) for 10 min at room temperature (RT). The appropriate amount of mRNA solution was diluted in Opti-MEM and incubated with LMM for at least 5 min at RT.

The hydrodynamic diameter of the NPs was measured at 25 °C by dynamic light scattering (DLS) using a Zetasizer Nano ZS (Malvern Instruments, Worcestershire, UK) equipped with a 4 mW He-Ne laser (633 nm) with a backscatter detection angle of 173°. Alternatively, mRNA NPs were measured using a NANO-flex (Microtrac MRB, Montgomeryville, PA, USA) at an angle of 180°, using a 3 mW 780 nm laser line.

2.4. mRNA (Co–)transfections

One day before mRNA transfections, 10,000 MC3T3 cells in 100 μL were seeded in 96-well plates (Greiner Bio-One Cat. No. 655180), or 20,000 cells in 200 μL in μ-slide 8-well chambers (Ibidi, Gräfelfing, Germany). These seeding densities ensured confluency between ~ 70–90 % on the day of transfection. mRNA transfections were performed by removing the complete medium from the wells and replacing it with mRNA NPs diluted ten times in complete medium. In a humidified incubator, cells were exposed to mRNA NPs for 2 h at 37 °C, 5 % CO_2. For some experiments, cells were stained with 200 μL 50 nM LysoTracker Green DND-26 (Thermo Fisher Scientific, Cat. No. L7526) directly after the NP incubation, according to the manufacturer's instructions.

Regardless of the tested N/P ratio or peptide, mRNA inputs were equalized across conditions, resulting in 107 ng per well for luciferase assays in 96-well plate formats and 214 ng per well for confocal microscopy experiments. Notably, these amounts of mRNA ensured equal doses (pg mRNA/cell) regardless of the format used for transfection. This excludes the 5 μM R9 conditions, which had a 4.6 times higher amount of mRNA. Only complete cell culture medium was added for untreated controls and refreshed as often as in the experimental conditions. Simultaneous transfections were carried out by the simultaneous addition of both transfection agents in a μ-slide 8-well chambers (Ibidi). For staggered co-transfections, cells were first transfected with either R9-eGFP or PF14-mCherry mRNA NPs for 30 mins, washed twice with PBS, and transfected for 2 h with the other mRNA NP.

2.5. Live-cell confocal laser scanning microscopy (LCLSM)

Prior to LCLSM, complete medium containing phenol red was replaced with an equal volume of phenol red-free Opti-MEM (Gibco, Cat No. Cat. No. 11058021), supplemented with 10 % PBS and 20 mM HEPES pH 7.4. The uptake of fluorescently labeled mRNA NPs was assessed two hours post-transfection, and reporter protein expression was assessed 24 h post-transfection. Live-cell imaging was performed using a Leica TCS SP8 SMD (Leica Microsystems, Mannheim, Germany) with an HC PL APO CS2 63×/1.20 water objective lens and a temperature-controlled stage at 36.5 °C. All laser lines were generated by a white-light laser and emissions were detected with hybrid detectors.

Alternatively, for higher resolution imaging, confocal images were collected using a Zeiss LSM 900 confocal system fitted with an Airyscan 2 module, mounted on an inverted Zeiss Axio Observer Z1 microscope with a Plan-Apochromat 63x/1.4 DIC M27 oil objective lens. The optimal setting (Nyquist sampling) suggested by Zeiss for the number of pixels in the x-y direction (40 nm per pixel) was used for all images, which were acquired in Airyscan mode (super-resolution) using a 32-channel gallium arsenide phosphide photomultiplier tube (GaAsP-PMT). The Zeiss ZEN 3.4 (blue) software package was used for collection and postprocessing of the images by using the 2D super-resolution setting with auto filter and standard strength. Regardless of the confocal setup, equal acquisition settings (pixel size, pinhole, laser power, and gain) per fluorophore were used within all experiments. eGFP or AF488 were excited at 488 nm (emission: 500–550 nm), mCherry and AF568 were excited at 561 nm (emission: 580–630 nm), and AF647 was excited at 633 nm (emission 650–690 nm). All channels were sequentially acquired to avoid crosstalk at a bit depth of 12.

2.6. Quantification of fluorescence intensities and degree of colocalization

Quantification of fluorescence was performed as previously described [45]. In brief, whole-image masks were analyzed using ImageJ (version 1.53f51) and used to calculate the raw integrated density, which is the sum of all pixels within a region of interest (ROI). To correct for differences in background fluorescence, a cell-free ROI was used to determine background fluorescence. To obtain the corrected total cellular fluorescence, the area (in pixels) was multiplied by the mean gray value of the background and subsequently subtracted from the raw integrated density of the ROI. For colocalization analysis of confocal microscopy data, we used the JACoP plugin combined with Costes' automatic threshold [8] to remove the bias of visual interpretation [46,47].

2.7. Detection of luciferase expression

According to the manufacturer's instructions, the extent of luciferase production was determined using the Nano-Glo Luciferase Assay (Promega, Madison, WI, USA, Cat No. N1130). Briefly, 50 μL of the sample was mixed with a 1:50 dilution of Nano-Glo luciferase assay substrate in Nano-Glo luciferase assay buffer. The resulting mixture was incubated at RT, hidden from light, for at least 3 min in a black transparent flat bottom 96-well plate (Corning Inc., Corning, NY, USA, Cat No. 3631). An inter-sample distance in the 96-well plate of at least two columns ensured no signal crosstalk between experimental conditions. Luminescence was measured after briefly shaking the plate using a VICTOR X3 Multilabel Plate Reader (Perkin Elmer, Waltham, MA, USA).

2.8. Electroporation of cells with mCherry-Galectin-9 plasmid DNA

An M6P-YFP-blasticidin-galectin-9 plasmid was obtained from Gisela Otten (Felix Randow Lab; MRC Laboratory of Molecular Biology, Cambridge, United Kingdom). We removed the YFP from this plasmid in favor of an N-terminal mCherry. Successful cloning of the N-terminal mCherry galectin-9 plasmid was confirmed by sequencing.

Before electroporation, 750,000 HeLa cells were resuspended in 100 μL pre-warmed RPMI without FBS containing 1.5 μg mCherry-galectin-9 pDNA. Immediately after resuspension, cells were transferred to a100 μL Nucleocuvette vessel and electroporated with a 4D-Nucleofector (Lonza Group AG, Basel, Switzerland) using the CN-114 program. After electroporation, cells were immediately diluted in complete RPMI and seeded in μ-slide 8-well chambers (Ibidi) at a density of 20,000 cells per well. 18 h after electroporation, cells were transfected with mRNA nanoparticles as described in 2.4.

2.9. Dual-color direct stochastic optical reconstruction microscopy (DC-dSTORM)

mRNA nanoparticles were prepared as described in section 2.3. 200 μL of NP solutions were pipetted on 25 mm coverslips thickness #1.5 (Electron Microscopy Sciences, Hatfield, PA, USA, Cat No. 72290-12) and incubated for 20 min at RT. Samples were fixed for 30 min in 4 % paraformaldehyde in 0.2 M PBS pH 7.4, supplemented with 0.1 % w/v glutaraldehyde. After thorough washing, remaining reactivity of the fixatives was quenched by a 30-min incubation with 100 mM glycine and 100 mM NH_4Cl (Sigma-Aldrich, Cat. No. 50046 and 213330, respectively) in PBS. Thereafter, the coverslips were placed in a custom-made low-drift magnetic sample holder filled with approximately 1 mL of OxEA buffer [48].

DC-dSTORM microscopy was performed in Wide-Field illumination mode using a custom-build low-drift inverted microscope setup equipped with a nanometer resolution xyz piezo stage (PInano P-545.3R7 Piezo System; Physik Instrumente, Karlsruhe, Germany). In the excitation path, three laser light sources were spatially overlapped: a 1000 mW 639 nm laser, a 500 mW 488 nm laser (Genesis MX STM OPSLaser System, Coherent), and a 100 mW 405 nm laser (OBIS LX Laser System, Coherent). These lasers were focused at the back focal plane of the imaging objective (APON 60XOTIRF /1.49 OIL, Olympus America Inc.). Emitted light was then focused using an achromatic lens (f:175 mm, Newport, PAC061AR.14) onto a scientific CMOS camera (ORCA-Flash4.0 V2, Hamamatsu). For dual-color imaging, the light was filtered using a triple band dichroic mirror (ZT405/488/635rpc, Chroma) in combination with an emission filter (FF01-565/133-25, Semrock and/or ET655lp, Chroma). The setup was controlled using custom-written software in MATLAB (MathWorks, Massachusetts, USA) [49].

During data acquisition, sample plane excitation power densities of ~ 1.5–2.0 kW/cm^2 were used for the 639 nm and 488 nm light sources, respectively. Imaging was performed separately for each channel, with the 639 nm channel imaged first. For each channel, a total of 5,000 × 10 = 50,000 frames were acquired within a region of interest of 300 × 300 pixels of 0.111 μm at an exposure time of 10 ms.

2.10. DC-dSTORM data processing

DC-STORM data were processed with ImageJ (version 1.52) using the ThunderSTORM plugin [50], which was automated using Supplementary Script 1**.** Images were reconstructed from 1-5x10^7 fit positions, with a detection threshold of 100–200 photons for the 488 nm and 639 nm channels, respectively. Typical uncertainty mode values were 11 nm for the 639 nm channel and 14 nm for the 488 nm channel (Fig. S10G). Image reconstruction was performed using the average shifted histograms method, with a rendering pixel size of 10 nm. A density kernel, with a distance radius of 55 and with a minimum of 5 neighbors in the radius, was applied for the 488 channel [51]. Software drift correction was performed for 639 channel data by a cross-correlation algorithm with ten bins, a smoothing factor of 0.35, and a magnification of 5.0.

Chromatic aberration shifts in the 488 channel were corrected using the Detection of Molecules plugin (available here: https://github.com/UU-cellbiology/DoM_Utrecht). The emission positions of the fiducials were determined using 2D Gaussian fitting at each recorded location. A locally weighted transformation between both channels was used [52], allowing the transfer of fits from the 488 to the 639 channel.

Separate channel localizations were merged into a single file using Supplementary Script 2 and automatically subdivided into smaller ROIs to minimize computational burden using Supplementary Script 3. Then, we used the Nanofeatures script (available here: https://github.com/crizloz/nanoFeatures, courtesy of Cristina Izquierdo-Lozano, Institute for Complex Molecular Systems (ICMS), Eindhoven University of Technology) to divide the ROI into 9 distinct sections, followed by density-based spatial clustering of applications with noise (DB-SCAN), while using a scanning diameter of 40 nm with a minimum of ten points (**Fig. S11**). After clustering, clusters with more than 2000 points or with an aspect ratio higher than 1.8 were removed. From these data, NP characteristics such as size, radius, number of localizations were extracted from each channel. For colocalization analysis of DC-dSTORM data, the number of overlapping localizations from each channel was normalized by the total number of localizations of in each channel with Supplementary Script 4.

2.11. Data analysis and statistics

Data analysis was performed using GraphPad Prism (GraphPad Software, version 8.4.2, San Diego, CA, USA). Data are presented as mean ± standard deviation (SD). Means were calculated by first averaging the technical replicates, for which outliers were identified using Grubbs' test, followed by averaging the biological replicates. Before statistical analysis, all data were checked for normal distribution with a Shapiro–Wilk test. Statistical analysis was done using one- or two-way analysis of variance (ANOVA). Multiple comparisons were corrected using Tukey's test with 95 % confidence intervals, unless stated otherwise; $p > 0.05$ was considered not significant (ns), and p values were reported using the GraphPad Prism style (* $p \leq 0.05$, ** $p \leq 0.01$, *** $p \leq 0.001$, and **** $p \leq 0.0001$).

3. Results

3.1. Cellular uptake of R9- and PF14-formulated mRNA nanoparticles

Although nona-arginine (R9) is a well-established cell-penetrating peptide (CPP), we have not been able to achieve RNA delivery for inducing protein downregulation with R9-formulated small interfering RNA (siRNA) or antisense oligonucleotide NPs [53,54]. Delivery efficiency is a function of the stability of particles in serum, cellular uptake, endosomal release, and finally, liberation of RNA inside the cytosol. Here, we sought to better understand the bottlenecks of R9-mediated delivery as a representative for an mRNA formulation that yields monodisperse NPs and shows uptake but no mRNA expression. For this purpose, R9-formulated mRNA NPs were co-transfected with mRNA NPs formulated with the efficient peptide-based carrier PepFect14 (PF14). To monitor the cellular uptake of mRNA NPs by confocal microscopy, we employed AF568- and AF647-labeled mRNA. In the first experiment, we confirmed that both mRNA NPs could be formed equally well, and intracellular fluorescence was also readily detected. Dynamic light scattering (DLS) confirmed that PF14-mRNA NPs formed with AF568- or AF647-labeled mRNA yielded intensity-based particle size distributions of 74.11 ± 5.78 nm and 64.11 ± 0.73 nm, respectively. R9-formulated mRNA NPs were slightly bigger but more monodisperse than those formed with PF14, where R9-AF568 mRNA NPs had a size of 97.33 ± 9.71 nm and R9-AF647 mRNA NPs of 86.30 ± 2.34 nm (**Fig. S1**). Salt, as present in the incubation medium may shield charges, potentially leading to particle aggregation. For this reason, we also performed measurements of PF14-mRNA nanoparticles in the presence of 150 mM NaCl (**Fig. S2**). There was some aggregation, however, the main fraction of particles retained the original size, consistent with microscopy where we also did not observe the presence of aggregates (see below).

R9-mRNA NPs were formulated with the same mRNA dose as PF14-mRNA NPs to enable fair comparisons of mRNA uptake efficiencies. At the same N/P ratio, which specifies the ratio of positive (nitrogen) over negative (phosphate) charge, an mRNA dose of 100 ng corresponded to final peptide concentrations of 2 μM for PF14 and 1.11 μM for R9. Additionally, we also included 5.16 μM R9-mRNA NPs. All conditions are thus given with respect to peptide concentration. Peptide-mediated cellular uptake of fluorescently labeled mRNA was assessed two hours after transfection. To assess endolysosomal trafficking, cells were additionally treated with LysoTracker. Free AF568 mRNA only yielded minimal uptake (Fig. 1A**,** Fig. S3A). For AF647 mRNA, the degree of uptake between free mRNA and formulated with 1 μM R9-647 were comparable. PF14-formulated mRNA showed pronounced cellular

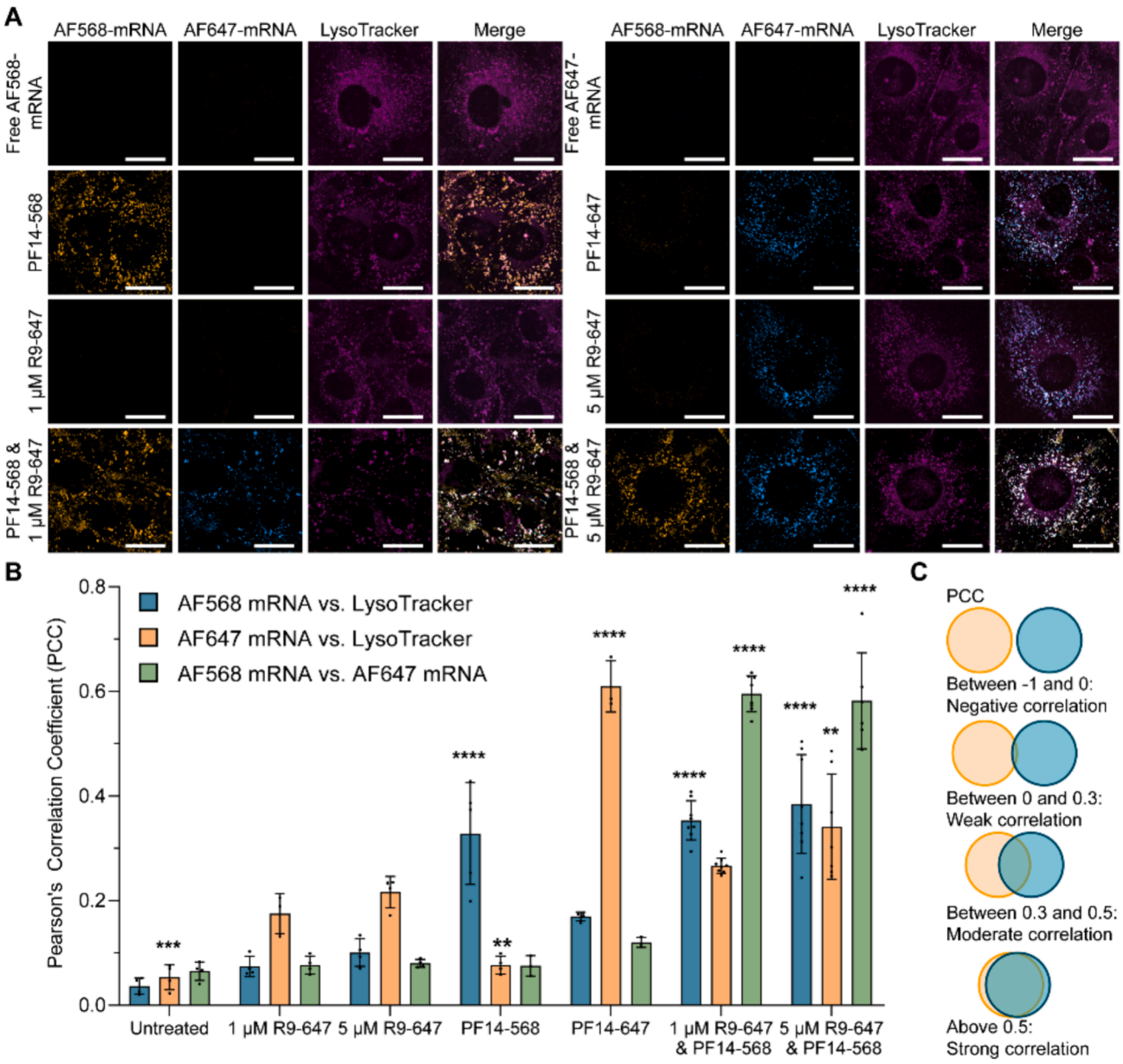

Fig. 1. Co-transfection of PepFect14 (PF14) and nona-arginine (R9) mRNA nanoparticles boost the uptake and lysosomal colocalization of R9-formulated mRNA. A) The effects of co-transfection on the uptake of fluorescently labeled mRNA and lysosomal colocalization. Uptake was assessed 2 h post-transfection using the Airyscan microscope. Brightness and contrast were equally adjusted across conditions per fluorophore, except for LysoTracker, which was automatically adjusted in ImageJ. Scale bars represent 25 μm. B) Quantification of Pearson's correlation coefficient (PCC) using JACoP[46] with Costes' automatic thresholding. Data represent the mean ± SD of 3–8 fields of view per channel. All conditions were compared to 5 μM R9-mRNA NPs per group, and only significant differences are depicted. C) Schematic depiction of PCC values and degree of correlation. Data were analyzed using one-way ANOVA, corrected with Dunnett's multiple comparisons test. ** $p \leq 0.01$, *** $p \leq 0.001$, and **** $p \leq 0.0001$.

uptake and punctate distribution of fluorescence that strongly colocalized with lysotracker irrespective of the nature of the fluorophore. The uptake of R9-formulated mRNA only reached significance, compared to the untreated conditions, by increasing the peptide and mRNA dose by a factor of five (Fig. S3B).

For co-transfections of 2 μM PF14-AF568 mRNA NPs and either 1 μM R9-AF647 mRNA NPs or 5 μM R9-AF647 mRNA NPs, the uptake of R9-AF647 mRNA NPs was significantly increased compared to R9-AF647 mRNA NPs alone as evident from confocal microscopy and supported by quantitative image analysis (Fig. 1A, Fig. S3**B**). Interestingly, co-incubation with 1 μM R9-AF647 mRNA NPs also increased the uptake of PF14-AF568 mRNA NPs, whereas co-incubation with 5 μM R9-AF647 mRNA NPs slightly decreased the AF568 signal (**Fig. S3A**). Overall, these results demonstrate that the presence of PF14-mRNA NPs substantially increased the uptake of R9-mRNA NPs but that, conversely, R9-mRNA NPs only had a minor effect on PF14-mRNA NPs.

Quantitative colocalization analyses revealed that when 5 μM R9-mRNA NPs were co-transfected with PF14-mRNA NPs, there was a significant increase in endolysosomal colocalization (Fig. 1B). Moreover, the Pearson's correlation coefficient (PCC; Fig. 1C) of ~ 0.6 for the 5 μM R9-AF647 mRNA NPs & PF14-AF568 mRNA NPs implies that the majority of both types of mRNAs NPs colocalize. These results strongly suggest that, when co-transfected, R9- and PF14-mRNA NPs reach the same endocytic compartments.

3.2. Co-transfection with PF14 induces the expression of R9-formulated mRNA

We and others have previously shown that cellular uptake of mRNA NPs has insufficient predictive power for cytosolic mRNA delivery [55,56]. Therefore, we sought to determine whether the enhanced colocalization of R9-formulated mRNA with endocytic compartments in co-transfections with PF14-mRNA NPs would also yield expression of R9-formulated mRNA. Accordingly, we used PF14-eGFP mRNA NPs, PF14-mCherry mRNA NPs, and R9-eGFP mRNA NPs, which formed NPs of 47.98 ± 1.14 nm, 42.43 ± 0.59 nm, and 102.0 ± 0.61 nm, respectively (**Fig. S1**). Again, PF14 was formulated with both mRNAs to validate the expression of both reporter proteins as detected by confocal microscopy 24 h post-transfection using live-cell confocal microscopy (Fig. 2A).

By comparison, neither free mRNA nor R9-formulated mRNA produced detectable reporter protein expression. Importantly, co-transfection with PF14-mRNA NPs led to a significant increase in eGFP expression for both 1 μM R9-eGFP mRNA NPs and 5 μM R9-eGFP mRNA NPs. For PF14-mCherry mRNA NPs, the transfection efficiency was reduced when co-transfected with 1 or 5 μM R9-eGFP mRNA NPs (Fig. 2B). At least for co-transfection with 5 μM R9-mRNA NPs, this observation is consistent with the reduced uptake.

To solidify the evidence for the crucial role of PF14-mRNA NPs in enabling the expression of R9-formulated mRNA, we performed a dose-titration of PF14-mRNA NPs for both 1 and 5 μM R9-Luc mRNA NPs. There was a positive correlation of expression of 1 μM R9-Luc mRNA NPs for co-transfections with doses of PF14-mCherry mRNA NPs ranging from 1 to 2 μM PF14-mCherry mRNA NPs ($R^2 = 0.56$) with lower concentrations of PF14 NPs not showing an effect (Fig. S4A). For co-transfections with 5 μM R9-Luc mRNA NPs, the R^2 value increased to 0.91 (**Fig. S4B**). Moreover, co-transfections with 5 μM R9 mRNA NPs were more robust than those with 1 μM R9 mRNA NPs, as evidenced by the increased significance of differences between conditions. We

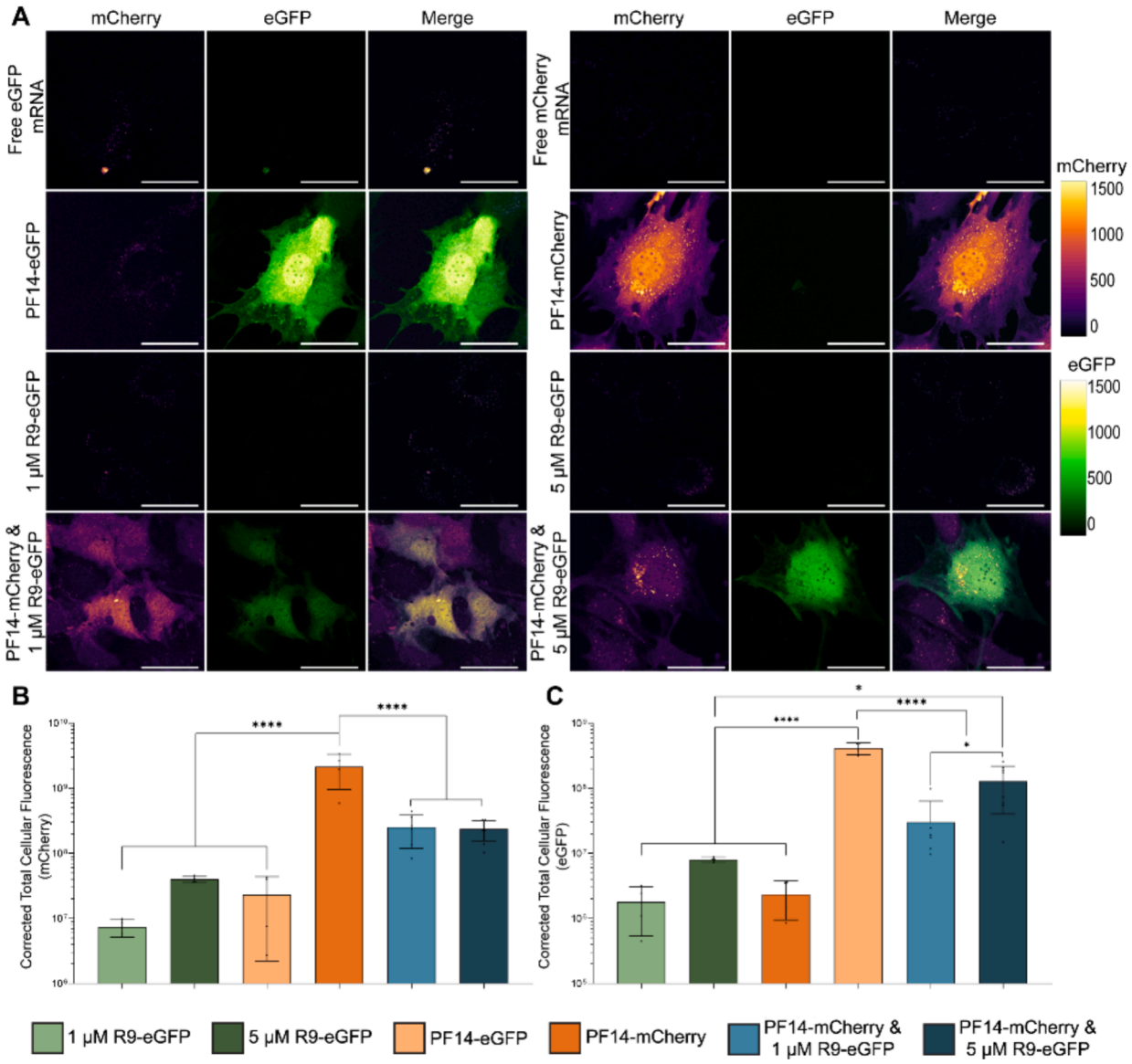

Fig. 2. Co-transfection of PF14- and R9-mRNA nanoparticles yields expression of R9-formulated eGFP mRNA. A) The effects of co-transfection on the expression of PF14-formulated mRNA (mCherry) and R9-formulated mRNA (eGFP). Expression was assessed 24 h post-transfection using the Airyscan microscope. Brightness and contrast were equally adjusted across conditions per fluorophore, according to the calibrated look-up tables (right), where the values reflect pixel intensities. Scale bars represent 50 μm. **B**) Quantification of mCherry fluorescence, and **C**) eGFP expression. The color-coded boxes beneath the panels represent the different conditions. Data represent the mean ± SD of 4–8 fields of view per channel. Data were analyzed using one-way ANOVA, corrected with Tukey's multiple comparisons test. Only significant differences are depicted. * $p \leq 0.05$, ** $p \leq 0.01$, *** $p \leq 0.001$, and **** $p \leq 0.0001$.

confirmed that over the tested ranges, viability of cells was preserved. Viability was compromised as soon as cells were incubated with 4 μM PF14-NPs (Fig. S4**C**). All experiments were conducted in the presence of serum as this mimics the physiological protein environment more closely. Also in the absence of serum, there was no protein expression from R9-mRNA nanoparticles whereas expression was observed for co-transfections (Fig. S5).

3.3. *Only simultaneous co-transfection of PF14 and R9 yields mRNA delivery benefits*

Next, we explored different co-transfection protocols to bolster our hypothesis that endosomal co-entrapment of PF14 and R9 enabled the expression of R9-formulated mRNA. So far, co-transfections were performed by simultaneously adding separately formulated mRNA particles to cells (synchronous co-transfection) and incubating for 2 h. We suspected that the uptake kinetics of both mRNA carriers should be sufficiently matched for co-transfections to yield endosomal co-entrapments with subsequent expression of two mRNAs present in separately formulated NPs. Therefore, we tried 30 min R9-eGFP incubation followed by 2 h of PF14-mCherry incubation and vice versa (staggered co-transfection).

These modified co-transfection protocols revealed that expression of the R9-formulated eGFP mRNA was only achieved when PF14 and R9 mRNA NPs were simultaneously added to cells. In contrast, regardless of transfection protocol, mCherry levels were similar across conditions (Fig. S6, Fig. S7**A&B**). Additionally, we included conditions containing free mRNA and free peptide to control for spontaneous formation of mRNA NPs. However, we found that none of the conditions yielded any detectable fluorescent reporter protein expression (Fig. S7**C&D**). These data clearly indicate that PF14 NPs must be co-transfected with R9 NPs simultaneously to facilitate sufficient endosomal co-entrapment to enable the endosomal escape of R9-formulated mRNA.

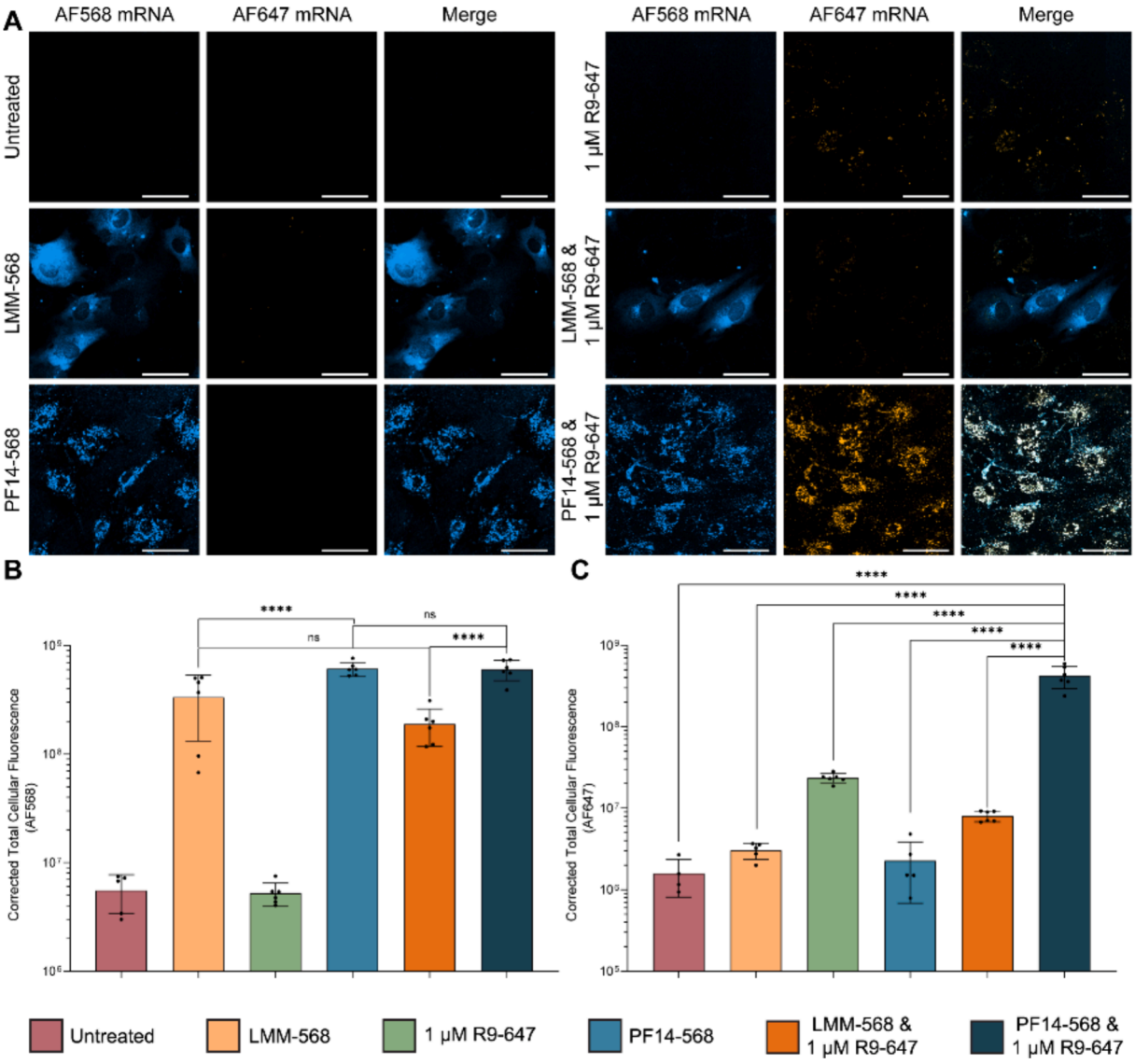

Fig. 3. LMM does not facilitate higher mRNA uptake or enable the expression of R9-formulated mRNA. A) The effects of co-transfections with LMM-AF568 mRNA NPs or PF14-AF568 mRNA NPs with R9-AF647 mRNA NPs on the uptake of R9-formulated mRNA. Uptake was assessed 2 h post-transfection; the scale bars represent 50 μm. **B**) Quantification of AF568-labeled mRNA, and **C**) AF647-labeled mRNA. The color-coded boxes beneath the panels represent the different conditions. Data represent mean ± SD of three biological replicates. Data were analyzed using one-way ANOVA, corrected with Tukey's multiple comparisons test. ns: non-significant, **** $p \leq 0.0001$.

3.4. A shared uptake route of mRNA carriers is a prerequisite for expression enhancement through co-transfection

Both R9 and PF14 are cell-penetrating peptides that mediate NP uptake through induction of endocytosis [57,58]. Thus, we next investigated co-transfection of R9-mRNA NPs with the lipid-based transfection agent Lipofectamine MessengerMAX (LMM) to probe for shared uptake routes. Previously, we have shown that LMM has faster mRNA uptake kinetics, resulting in a more homogeneous cytoplasmic distribution of mRNA and less endosomal entrapment [43,59]. Despite these uptake characteristics, delivery of PF14-formulated mRNA resulted in more cellular uptake of mRNA than LMM in terms of fluorescence intensities [55].

Using live-cell confocal microscopy, it became apparent that LMM did not harbor the same ability as PF14 to boost the uptake of R9-mRNA NPs (Fig. 3A**)**. Co-transfection of LMM and R9-mRNA NPs neither decreased the uptake of LMM-formulated mRNA (Fig. 3B) nor did it increase the uptake of R9-formulated mRNA (Fig. 3C). There was, however, a mutual influence of particles at the level of luciferase expression (**Fig. S8**), which escaped the notion when assessing mRNA uptake by fluorescence. We attribute this observation to the sensitivity of the luciferase assay. In line with this observation, co-transfection of neither 1 μM nor 5 μM R9-formulated luciferase mRNA with LMM-mCherry mRNA resulted in any significant luciferase expression. However, co-transfections of 1 μM or 5 μM of R9-eGFP combined with LMM-Luc lead to significant decreases in luciferase expression, indicating that R9 co-transfections negatively affect LMM.

3.5. PF14 co-transfections robustly induce the expression of R9-formulated mRNA in multiple cell lines

The efficacy of a transfection agent for mRNA delivery strongly depends on the cell type. It can vary widely across primary and secondary cell lines, both from human and murine origin [60]. To assess the validity of co-transfection across cell lines, next to the murine pre-osteoblasts (MC3T3) used above, we also explored human epithelial cervical carcinoma cells (HeLa), human skin fibroblasts (C5120) and human bone marrow-derived mesenchymal stem cells (hBMSCs).

All tested cell lines showed robust luciferase expression induced either by PF14-formulated luciferase mRNA or when R9-formulated luciferase mRNA was co-transfected with PF14-mRNA NPs (Fig. 4). However, the extent of the co-transfection-mediated enhancement of luciferase activity strongly differed for the different cell lines, with C5120 cells showing the most substantial increase by a factor of 21,000 and MC3T3 cells showing the lowest enhancement by a factor of only 87.

3.6. PF14-mRNA NPs mediate endosomal rupture but show poor dissociation of nanoparticles

Whereas co-transfection of R9-mRNA NPs with PF14-mRNA NPs increased cellular uptake, induction of endosomal release is the prerequisite for mRNA expression. Expression of fluorescent protein-tagged

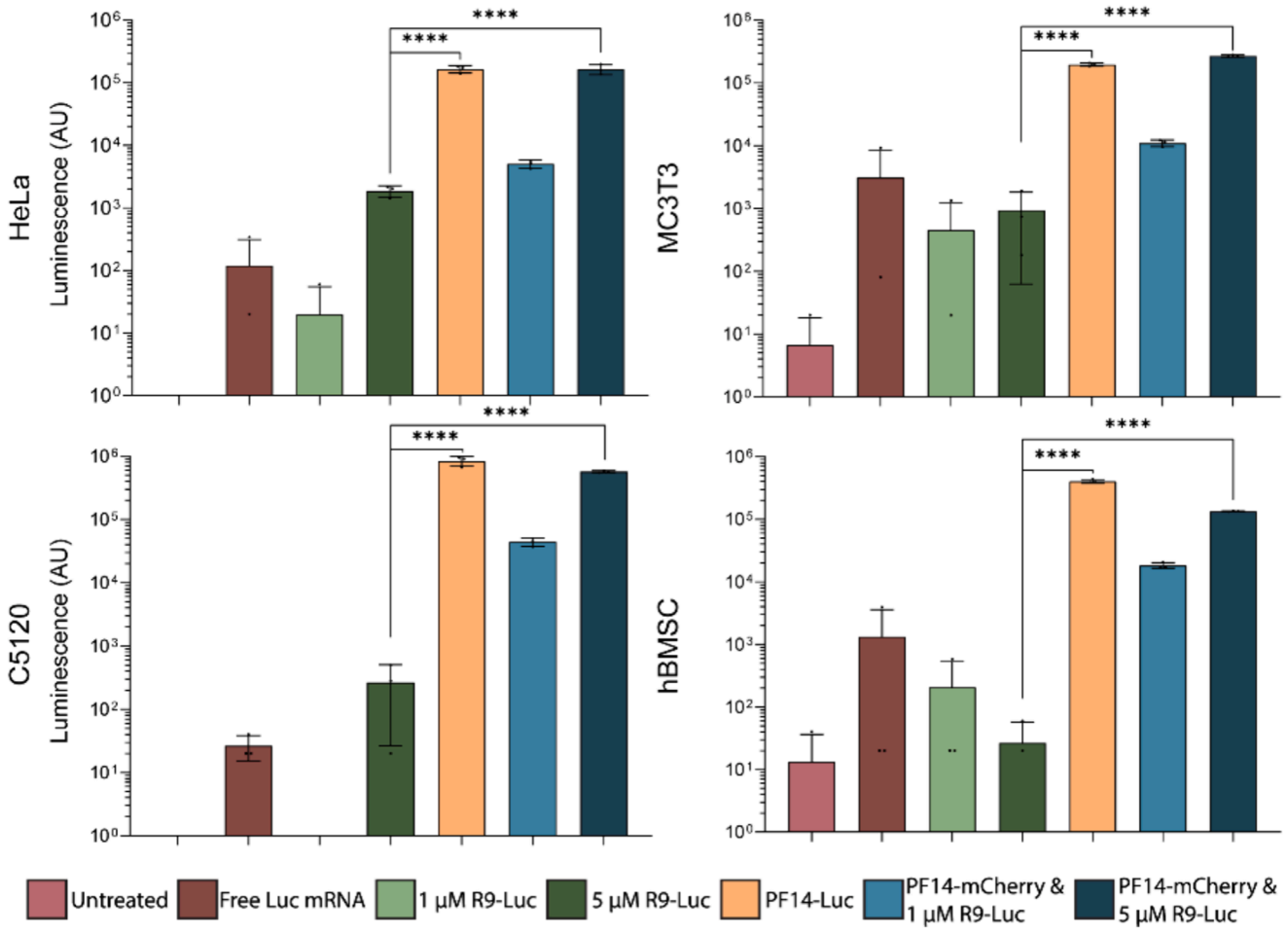

Fig. 4. The effects of mRNA co-transfections on luciferase expression in various cell lines. Quantification of luciferase expression 24 h post-mRNA transfection in **A**) HeLa cells, **B**) MC3T3 murine pre-osteoblastic cells, **C**) C5120 fibroblasts, and **D**) human bone marrow-derived stem cells (hBMSC). The color-coded boxes beneath the panels represent the different conditions. Data represents the mean ± SD of triplicate wells and is representative of three independent experiments. Data were analyzed using one-way ANOVA, corrected with Tukey's multiple comparisons test. **** $p \leq 0.0001$.

lectins in the cytosol provides the means to detect endosomal rupture through exposure of lectin binding sites towards the cytosol, resulting in a punctate staining (Fig. 5A).

Cells transfected with galectin-9-mCherry the previous day were imaged by live-cell confocal microscopy after 2-h incubation with mRNA NPs. For cells transfected with R9 mRNA NPs, the galectin-9-mCherry signal remained cytosolically dispersed, regardless of the R9 dose tested (Fig. 5B). By comparison, when cells were transfected with PF14-mRNA NPs, the galectin-9 signal was redistributed into punctate foci that colocalized with the mRNA signal. Co-transfection of cells with both types of NPs led to colocalization of fluorescence of both mRNAs with galectin-9.

Surprisingly, the galectin-9-positive punctae were long-lived and detectable 24 h post-transfection (Fig. S9**A**). For a quantitative perspective, we analyzed the degree of colocalization between Gal-9-mCherry and the mRNA NPs 2 and 24 h post-transfection. For 1 μM R9-AF488 mRNA NPs co-transfected with PF14-AF647 mRNA, colocalization increased from 2 to 24 h (Fig. S9**B**). Correspondingly, also for PF14-AF647 mRNA NPs, either transfected alone or combined with 1 μM R9-AF488 mRNA NPs, there was significantly more colocalization with Gal-9-mCherry after 24 h in comparison to 2 h post-transfection (Fig. S9**C**). Moreover, the colocalization between both fluorescently labeled mRNAs also significantly increased between timepoints in the condition where PF14 mRNA NPs and 1 μM R9 mRNA NPs were co-transfected (Fig. S9**D**). The increased colocalization of mRNA 24 h post-transfection indicates that endosomal escape is not completed 2 h post-transfection. Importantly, these data collectively indicate that although PF14 is an efficient CPP that effectively disrupts endosomal membranes, the peptide poorly dissociates from the mRNA cargo following endosomal escape. Since low levels of homogenously distributed mRNA would be difficult to detect, at this point, we cannot determine which fraction of mRNA remained captured.

3.7. Dual-color direct stochastic optical reconstruction microscopy (DC-dSTORM) confirms the absence of mRNA exchange between PF14 and R9 NPs

Finally, we aimed to exclude that co-transfections were the results of the exchange of mRNA between nanoparticles. To visualize individual NPs at nanometer resolution, we employed dual channel (DC)-dSTORM. PF14 NPs were formulated with either AF488-labeled mRNA alone or with a mixture of AF488 and AF647 mRNA, while R9 NPs were formulated with AF647-labeled mRNA alone or a mixture of both mRNAs. This approach allowed us to benchmark the degree of overlap

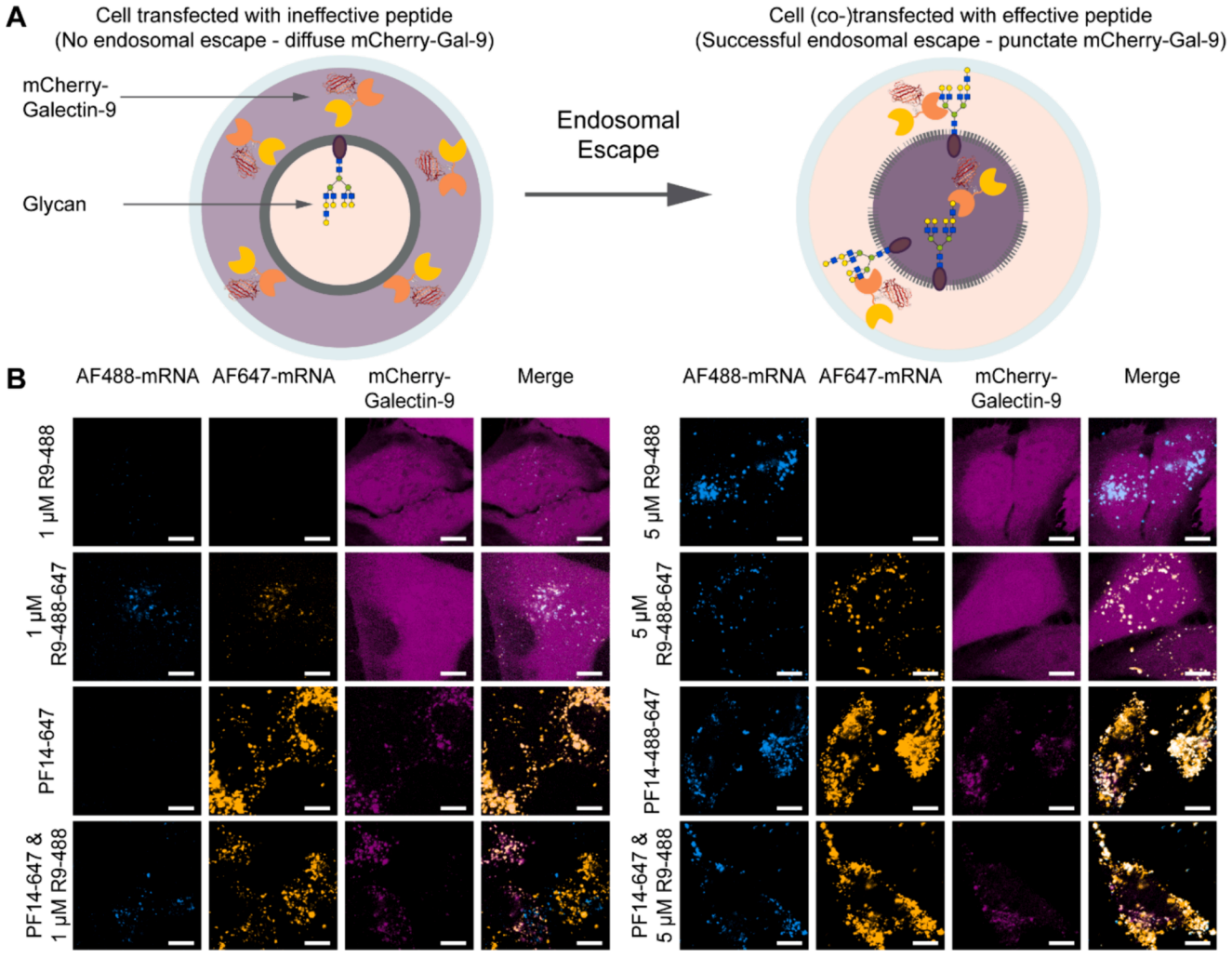

Fig. 5. Detection of endosomal disruption using mCherry-galectin-9 (mCherry-Gal-9) two hours post-transfection. A) In the resting state, mCherry-Gal-9 is homogenously distributed throughout the cytosol, resulting in a diffuse mCherry signal. Upon endosomal disruption, β-galactosides on the inner leaflet of endosomal membranes are exposed to the cytosol, leading to galectin-9 binding and resulting in a punctate mCherry-Gal-9 signal. **B**) Live-cell confocal microscopy of mRNA uptake 2 h post-transfection in HeLa cells electroporated with mCherry-Gal-9 pDNA (24 h pre-transfection). Brightness and contrast were equally adjusted across conditions for AF488 and AF647 signals. mCherry-galectin-9 signal was automatically adjusted in FIJI. Scale bars represent 10 μm.

between two fluorescently labeled mRNAs formulated within the same nanoparticle and compare it to the co-occurrence of two mRNAs formulated with separate peptides.

To identify and characterize NPs, we applied strategies as described before [17,61], and the quality of the DC-dSTORM data was validated with descriptive statistics (**Fig. S10A-G**). With our DC-dSTORM approach, we could readily detect nanoparticles, regardless of the peptide used for encapsulation of mRNA and regardless of the identity of the fluorescently labeled mRNA. Moreover, our results with R9 were similar to those previously reported with dSTORM [61].

For PF14-AF488 mRNA NPs, thus in the absence of a specific AF647 signal, the degree of colocalization with AF647 was negligible (0.307 ± 0.011 %), while for PF14-AF488-AF647 NPs, colocalization was 23.9 ± 0.762 % (**Fig. S10H**). By comparison, for R9 co-formulated with both mRNAs, there was no evidence for colocalization, even though each individual mRNA cluster could be detected. On one hand, these discrepancies may be due to the number of obtained clusters. For double-labeled PF14 NPs, we obtained 35 % more clusters in the AF647 channel than in the AF488 channel. Meanwhile, for double-labeled R9 mRNA NPs, we obtained 2.7 times more clusters in the AF488 channel compared to the AF647 channel. On the other hand, previous studies had shown only about three mRNA per NP [28,61]. Thus, at low total mRNA numbers per NP, only a fraction of NPs may contain both mRNAs. Still, partially overlapping clusters were present in images of both PF14-AF488-AF647 mRNA and R9-AF488-AF647 mRNA NPs (Fig. 6).

Importantly, no such overlap was observed in images of PF14-AF488 mRNA NPs and R9-AF647 mRNA NPs alone and of the co-deposition of both NPs, validating the absence of NP interactions and mRNA exchange. These results were bolstered by quantitative analyses of colocalization, which revealed that for co-deposited PF14-AF488 mRNA NPs and R9-AF647 mRNA NPs, only 1.16 % of the clusters colocalized, which is much less than the 23.9 % colocalization of the PF14-AF488-AF647 NPs. Additionally, the co-deposited PF14-AF488 mRNA NPs and R9-AF647 mRNA NPs showed a significantly lower amount of colocalized clusters than R9-AF647 mRNA NPs and R9-AF488-AF647 mRNA NPs (**Fig. S10**).

4. Discussion

Cytosolic delivery of oligonucleotides is a multi-step process and activity is only observed if all hurdles are overcome. Here, we showed that co-transfection of carriers provides a highly informative means to identify delivery bottlenecks and provide information on delivery routes.

Although R9 is a well-established CPP, there is little experimental support for its capacity to deliver (m)RNA [53]. Attempts to improve R9 delivery by incorporating histidines into the sequence only yielded benefits when the mRNA NP was coated with the cationic lipid DOTAP

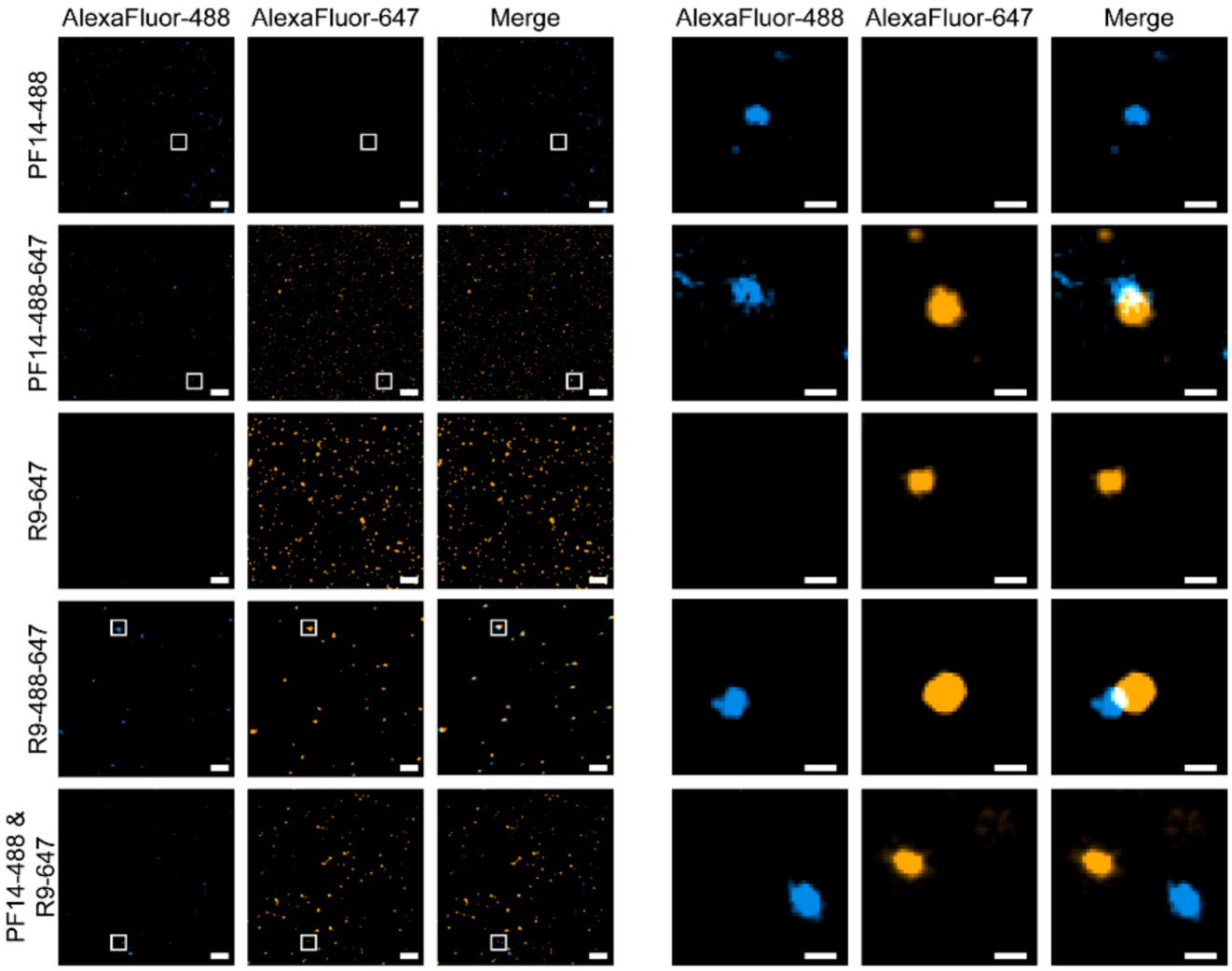

Fig. 6. Dual-color direct stochastic optical reconstruction microscopy (DC-dSTORM) average shifted histogram-reconstructed images of representative peptide-mRNA nanoparticles deposited on glass. Scale bars in left panels represent 1 μm; right panels 0.1 μm. Boxes in right panels represent the zoomed-in regions of interest in the left panels.

[62], or modified with reducible cysteines [63]. In contrast, stearylation of R9 was also not able to induce splice correction even in the presence of the endosomolytic agent chloroquine [64]. By comparison, PF14 yields more effective uptake and endosomal release. As we showed recently, the activity can be attributed to its amphipathic structure [55]. Positive charge alone is sufficient for complexing mRNA but fails in inducing cellular uptake and fully lacks the capacity to induce endosomal release.

Co-transfection of R9-mRNA NPs with PF14-mRNA NPs enabled the expression of R9-formulated mRNA. On the one hand, cellular uptake increased; on the other hand, co-transfection overcame the endosomal escape bottleneck of R9. Importantly, once inside the cytosol, R9-NPs released mRNA to a sufficient degree to enable translation. Also, the PF14-mRNA NP-mediated induction of protein expression from R9-mRNA NPs demonstrates that mRNA is effectively shielded from nuclease-mediated degradation. Remarkably though, not all cells co-expressed the R9 NP-delivered mRNA along the PF14 NP-delivered mRNA. This discrepancy may reflect differences to release mRNA from the nanoparticles. Furthermore, it has been shown before that co-delivery of two types of nanoparticles does not yield co-expression of proteins across all cells [65].

Detection of endosomal rupture by expression of galectin-9-mCherry yielded highly interesting results. Surprisingly, punctate galectin-9 signals were not transient but persisted for over 24 h. In addition, colocalization of the mRNA signals with Gal9-mCherry was higher at 24 h than at 2 h, indicating that over the 24 h, further endosomal rupture occurred. This result conflicts with the expectation that NPs should be sequestered in lysosomes at this late time point. However, with respect to intracellular trafficking, induction of autophagy and sequestration in autophagolysosomes has been reported for PF14 complexes [66]. Further research is needed to understand to which degree this localization relates to galectin-9-positive events.

For LNP-mediated delivery, it has been shown that endosomal release only occurs during a short time window of early endosomal passage [38]. At the same time, PF14-mRNA NPs only stimulated the endosomal release of R9-mRNA NPs upon co-incubation. This observation is also difficult to reconcile with increased endosomal rupture after 24 h as endosomal contents are expected to mix in late endosomes at this time point. The long-lived galectin-9 signal warrants future research into the endolysosomal fine structures and how they relate to the localization of mRNA NPs. For assessment of potential particle toxicity it will be highly relevant to understand whether these endosomes are still ruptured or whether galectin-9 remains bound to exposed glycolipids. Correlative fluorescence/cryo-electron microscopy would be the method of choice [67]. We also learned that, unlike previously assumed, the punctate distribution of mRNA fluorescence is not due to mRNA sequestration in intact endolysosomes but instead mRNA NPs are associated with ruptured vesicles. This observation also explains why nuclear fluorescence was observed for PF14-delivered fluorescently labeled antisense oligonucleotides, even though most signals were still punctate [54]. It will be highly interesting to investigate whether mRNA translation also happens close to these structures or from a small fraction of mRNA released from these structures [68].

Persistent punctate structures indicate a highly relevant difference between the cell-penetrating peptides and lipid nanoparticles (LNPs) as delivery vehicles. Crucial for LNP activity are protonatable lipids with a pKa around 6. LNPs are formed at a slightly acidic pH at which the protonatable lipids are positively charged and able to complex (m)RNA. At neutral pH, positive charges at the surface are neutralized. Protonation inside the endosomes promotes interactions with negatively charged lipids of the endosomal membrane, which drives LNP dissociation and endosomal rupture. Thus, LNPs possess an environmental sensitivity that drives dissociation. By comparison, the CPP NPs used in our study lack such environmental responsiveness. For CPPs, strategies that have been explored to liberate the mRNA from its carrier, following endosomal escape, incorporate a bioreducible element in the CPP, such as disulfide bonds that are quickly reduced by intracellular glutathione or pH-responsive elements such as histidines, which are protonated within the endosome but lose their charge once present cytosolically [69,70]. It will be intriguing to revisit these strategies in combination with the galectin-9 assay to assess whether sequestration at ruptured endosomes is indeed reduced.

Co-transfection efficiency was observed across a panel of cell lines, even though the extent differed. Co-transfections yielded two orders of magnitude higher luciferase expression in HeLa and MC3T3 cells and over three orders of magnitude for C5120 and hBMS cells. Potentially, these differences could relate to the different capacities of PF14 to induce endocytosis.

Interestingly, co-incubation with lipofectamine-formulated mRNA failed to enhance the uptake of R9 NPs. Consistently, for LMM-mediated mRNA uptake, we observed a homogenous cytosolic distribution of mRNA, indicating minimal endosomal capture and most likely implying a delivery pathway that involves direct fusion of lipid micelles with the plasma membrane [55]. Others have, however, observed a release from endosomal structures [71]. Also co-incubation with PF14 alone did not yield R9-mRNA delivery. PF14 has only been investigated in the context of oligonucleotide nanoparticles. Thus, no data is available whether PF14 alone enters via a different route than PF14-mRNA nanoparticles.

Next to yielding a mechanistic understanding of delivery bottlenecks, we can also envision a potential applied aspect in the co-delivery of RNAs. Whereas strategies typically incorporate different oligonucleotides simultaneously into one vector, our results suggest that a poorly released vector A can be combined with an efficient vector B, yielding conditional delivery of A only in the presence of B. The general feasibility of this concept has been demonstrated for combination of lipid nanoparticle-formulated mRNA that reaches the liver but does not mediate endosomal release with liver-targeted polymer micelles that disrupt the endosomes [72]. However, in our case, co-administration of R9-mRNA nanoparticles with PF14 alone which also forms micelles was insufficient to drive endosomal release (Fig. S7D).

Lastly, we probed the possibility of mRNA exchange between PF14 and R9 NPs at single molecule resolution using DC-dSTORM. Again, we used NPs with two distinct, fluorescently labeled mRNAs to benchmark the degree of colocalization if two mRNAs are present in the same NP. Both visual inspection and quantification of colocalization pointed towards the absence of mRNA exchange between PF14 and R9 mRNA NPs. While NPs containing two distinct mRNAs were characterized by partially overlapping clusters, NPs containing one mRNA or co-deposition of PF14 and R9 mRNA NPs were characterized by mutually exclusive clusters. In unison, these data indicate no detectable mRNA exchange between separately formulated and co-deposited mRNA NPs.

Overall, we present a co-transfection strategy to identify bottlenecks in inefficient mRNA carriers by combining them with an efficient carrier. If co-transfections yield protein expression of the mRNA encapsulated by an inefficient carrier, which also shows uptake by itself, the endosomal escape is the main bottleneck. All preceding steps in mRNA delivery, ranging from extracellular stability and uptake inefficiencies, can be ruled out. This approach should aid the rational design and optimization of intracellular mRNA delivery systems.

Declaration of Generative AI and AI-assisted technologies in the writing process

While preparing this work, the authors used GPT-4 for language editing. Subsequently, the authors thoroughly reviewed and made necessary edits to the content, assuming full responsibility for the final publication.

CRediT authorship contribution statement

Rik Oude Egberink: Writing – review & editing, Writing – original draft, Visualization, Supervision, Methodology, Investigation, Formal analysis, Conceptualization. **Deni M. van Schie:** Visualization, Software, Investigation. **Ben Joosten:** Software, Methodology. **Lisa.T.A. de**

Muynck: . Ward Jacobs: Investigation. **Jenny van Oostrum:** Supervision, Methodology, Investigation. **Roland Brock:** Writing – review & editing, Supervision, Methodology, Funding acquisition, Conceptualization.

Declaration of Competing Interest

The authors declare the following financial interests/personal relationships which may be considered as potential competing interests: R. B. is a co-founder of Mercurna and RIBOPRO, companies that develop mRNA therapeutics (Mercurna) and offer mRNA services (RIBOPRO). The funders had no role in the study's design, in the collection, analyses, or interpretation of data, in the writing of the manuscript, or in the decision to publish the results.

Data availability

The data that support the findings of this study are available from the corresponding author upon reasonable request.

Acknowledgements

We thank L. Albertazzi ((Department of Biomedical Engineering, Institute for Complex Molecular systems (ICMS), Eindhoven University of Technology)) for helpful discussions regarding dual-color dSTORM acquisition and quality control, and C. Izquierdo Lozano (ICMS, TU/e) for sharing custom scripts for dSTORM image analysis. We are grateful for the input of G.-J. Bakker, S. van Deventer, and F. Schwerdtfeger (Dept. of Medical BioSciences, Radboudumc) regarding dual-color dSTORM image acquisition and analysis. M. van Erp is thanked for his assistance with in writing and automating the DC-dSTORM script. We thank P. Hagemann (Dept. of Medical BioSciences, Radboudumc) for assistance during electroporation experiments. The authors thank C.-A. Suurmond and R. Heesakkers (Dept. of Dentistry, Radboudumc) for providing and characterizing the human bone marrow-derived mesenchymal stem cells. Some graphical elements are adapted from Servier medical art repository (https://smart.servier.com) to prepare the graphical abstract and Fig. 6. Servier Medical Art by Servier is licensed under a Creative Commons Attribution 3.0 Unported License (https://creativecommons.org/licenses/by/3.0/). The Blue, Orange, and Purple look-up tables used in Fig.s 1, 3, and 5 were obtained from: https://github.com/cleterrier/ChrisLUTs. The authors wish to thank the Radboudumc Technology Center Microscopy for the use of their facilities. R. O.E. was supported by the Dutch Science Foundation (NWO TTW 17615).

Appendix A. Supplementary material

Supplementary data to this article can be found online at https://doi.org/10.1016/j.ejpb.2024.114414.

References

[1] L. Schoenmaker, D. Witzigmann, J.A. Kulkarni, R. Verbeke, G. Kersten, W. Jiskoot, D.J.A. Crommelin, mRNA-lipid nanoparticle COVID-19 vaccines: Structure and stability, Int. J. Pharm. 601 (2021) 120586.
[2] S.F. Dowdy, R.L. Setten, X.S. Cui, S.G. Jadhav, Delivery of RNA therapeutics: the great endosomal escape!, Nucleic Acid Ther. 32 (2022) 361–368.
[3] M. Kamiya, M. Matsumoto, K. Yamashita, T. Izumi, M. Kawaguchi, S. Mizukami, M. Tsurumaru, H. Mukai, S. Kawakami, Stability study of mRNA-lipid nanoparticles exposed to various conditions based on the evaluation between physicochemical properties and their relation with protein expression ability, Pharmaceutics 14 (2022).
[4] E. Oude Blenke, E. Ornskov, C. Schoneich, G.A. Nilsson, D.B. Volkin, E. Mastrobattista, O. Almarsson, D.J.A. Crommelin, The storage and in-use stability of mRNA vaccines and therapeutics: not a cold case, J. Pharm. Sci. 112 (2023) 386–403.
[5] S. Ndeupen, Z. Qin, S. Jacobsen, A. Bouteau, H. Estanbouli, B.Z. Igyártó, The mRNA-LNP platform's lipid nanoparticle component used in preclinical vaccine studies is highly inflammatory, iScience, 24 (2021) 103479-103479.
[6] N. Pardi, S. Tuyishime, H. Muramatsu, K. Kariko, B.L. Mui, Y.K. Tam, T.D. Madden, M.J. Hope, D. Weissman, Expression kinetics of nucleoside-modified mRNA delivered in lipid nanoparticles to mice by various routes, J. Control. Release 217 (2015) 345–351.
[7] M. Packer, D. Gyawali, R. Yerabolu, J. Schariter, P. White, A novel mechanism for the loss of mRNA activity in lipid nanoparticle delivery systems, Nat. Commun. 12 (2021) 6777.
[8] K.A. Hajj, K.A. Whitehead, Tools for translation: non-viral materials for therapeutic mRNA delivery, Nat. Rev. Mater. 2 (2017) 1–17.
[9] R. Feng, A.C.Y. Chang, R. Ni, J.C.Y. Li, Y. Chau, mRNA Delivery and storage by co-assembling nanostructures with designer oligopeptides, ACS Appl Bio Mater 5 (2022) 3476–3486.
[10] L. Opsomer, S. Jana, I. Mertens, X. Cui, R. Hoogenboom, N.N. Sanders, Efficient in vitro and in vivo transfection of self-amplifying mRNA with linear poly (propylenimine) and poly(ethylenimine-propylenimine) random copolymers as non-viral carriers, J. Mater. Chem. B 12 (2024) 3927–3946.
[11] H. Wang, X. Liu, X. Ai, K.C. Remant-Bahadur, T.A. Dick, B. Yan, T. Lu, X. Zhou, R. Luo, M. Liu, X. Wang, K. Li, W. Wang, H. Uludag, W. Fu, Safe and effective delivery of mRNA using modified PEI-based lipopolymers, Pharmaceutics 15 (2023).
[12] L.I. Selby, C.M. Cortez-Jugo, G.K. Such, A.P.R. Johnston, Nanoescapology: progress toward understanding the endosomal escape of polymeric nanoparticles, Wiley Interdiscip. Rev. Nanomed. Nanobiotechnol. 9 (2017).
[13] A. Yen, Y. Cheng, M. Sylvestre, H.H. Gustafson, S. Puri, S.H. Pun, Serum nuclease susceptibility of mRNA cargo in condensed polyplexes, Mol. Pharm. 15 (2018) 2268–2276.
[14] A. Dirisala, S. Uchida, T.A. Tockary, N. Yoshinaga, J. Li, S. Osawa, L. Gorantla, S. Fukushima, K. Osada, K. Kataoka, Precise tuning of disulphide crosslinking in mRNA polyplex micelles for optimising extracellular and intracellular nuclease tolerability, J. Drug Target. 27 (2019) 670–680.
[15] J.J. Rennick, A.P.R. Johnston, R.G. Parton, Key principles and methods for studying the endocytosis of biological and nanoparticle therapeutics, Nat. Nanotechnol. 16 (2021) 266–276.
[16] S.F. Dowdy, Endosomal escape of RNA therapeutics: how do we solve this rate-limiting problem? RNA 29 (2023) 396–401.
[17] P. Paramasivam, C. Franke, M. Stoter, A. Hoijer, S. Bartesaghi, A. Sabirsh, L. Lindfors, M.Y. Arteta, A. Dahlen, A. Bak, S. Andersson, Y. Kalaidzidis, M. Bickle, M. Zerial, Endosomal escape of delivered mRNA from endosomal recycling tubules visualized at the nanoscale, J. Cell Biol. 221 (2022).
[18] E.J. Sayers, S.E. Peel, A. Schantz, R.M. England, M. Beano, S.M. Bates, A.S. Desai, S. Puri, M.B. Ashford, A.T. Jones, Endocytic profiling of cancer cell models reveals critical factors influencing LNP-mediated mRNA delivery and protein expression, Mol. Ther. 27 (2019) 1950–1962.
[19] C.R. Brown, S. Gupta, J. Qin, T. Racie, G. He, S. Lentini, R. Malone, M. Yu, S. Matsuda, S. Shulga-Morskaya, A.V. Nair, C.S. Theile, K. Schmidt, A. Shahraz, V. Goel, R.G. Parmar, I. Zlatev, M.K. Schlegel, J.K. Nair, M. Jayaraman, M. Manoharan, D. Brown, M.A. Maier, V. Jadhav, Investigating the pharmacodynamic durability of GalNAc-siRNA conjugates, Nucleic Acids Res. 48 (2020) 11827–11844.
[20] C. He, M.T. Migawa, K. Chen, T.A. Weston, M. Tanowitz, W. Song, P. Guagliardo, K.S. Iyer, C.F. Bennett, L.G. Fong, P.P. Seth, S.G. Young, H. Jiang, High-resolution visualization and quantification of nucleic acid-based therapeutics in cells and tissues using Nanoscale secondary ion mass spectrometry (NanoSIMS), Nucleic Acids Res. 49 (2021) 1–14.
[21] G. Sahay, W. Querbes, C. Alabi, A. Eltoukhy, S. Sarkar, C. Zurenko, E. Karagiannis, K. Love, D. Chen, R. Zoncu, Y. Buganim, A. Schroeder, R. Langer, D.G. Anderson, Efficiency of siRNA delivery by lipid nanoparticles is limited by endocytic recycling, Nat. Biotechnol. 31 (2013) 653–658.
[22] K.B. Knudsen, H. Northeved, P.E. Kumar, A. Permin, T. Gjetting, T.L. Andresen, S. Larsen, K.M. Wegener, J. Lykkesfeldt, K. Jantzen, S. Loft, P. Moller, M. Roursgaard, In vivo toxicity of cationic micelles and liposomes, Nanomedicine 11 (2015) 467–477.
[23] A. Sukhanova, S. Bozrova, P. Sokolov, M. Berestovoy, A. Karaulov, I. Nabiev, Dependence of Nanoparticle toxicity on their physical and chemical properties, Nanoscale Res. Lett. 13 (2018) 44.
[24] D. Sun, Z.-R. Lu, Structure and function of cationic and ionizable lipids for nucleic acid delivery, Pharm Res-Dordr 40 (2023) 27–46.
[25] A.M. Jörgensen, R. Wibel, A. Bernkop-Schnürch, Biodegradable Cationic and Ionizable Cationic Lipids: A Roadmap for Safer Pharmaceutical Excipients, Small, n/a (2023) 2206968-2206968.
[26] A. Takanashi, C.W. Pouton, H. Al-Wassiti, Delivery and expression of mRNA in the secondary lymphoid organs drive immune responses to lipid nanoparticle-mRNA vaccines after intramuscular injection, Mol. Pharm. 20 (2023) 3876–3885.
[27] J.A. Kulkarni, D. Witzigmann, J. Leung, R. van der Meel, J. Zaifman, M.M. Darjuan, H.M. Grisch-Chan, B. Thony, Y.Y.C. Tam, P.R. Cullis, Fusion-dependent formation of lipid nanoparticles containing macromolecular payloads, Nanoscale 11 (2019) 9023–9031.
[28] S. Li, Y. Hu, A. Li, J. Lin, K. Hsieh, Z. Schneiderman, P. Zhang, Y. Zhu, C. Qiu, E. Kokkoli, T.H. Wang, H.Q. Mao, Payload distribution and capacity of mRNA lipid nanoparticles, Nat. Commun. 13 (2022) 5561.
[29] T.K. Kerppola, Visualization of molecular interactions using bimolecular fluorescence complementation analysis: characteristics of protein fragment complementation, Chem. Soc. Rev. 38 (2009) 2876–2886.
[30] N. Milech, B.A. Longville, P.T. Cunningham, M.N. Scobie, H.M. Bogdawa, S. Winslow, M. Anastasas, T. Connor, F. Ong, S.R. Stone, M. Kerfoot, T. Heinrich, K. M. Kroeger, Y.F. Tan, K. Hoffmann, W.R. Thomas, P.M. Watt, R.M. Hopkins, GFP-

complementation assay to detect functional CPP and protein delivery into living cells, Sci. Rep. 5 (2015) 18329.
[31] P. Lonn, A.D. Kacsinta, X.S. Cui, A.S. Hamil, M. Kaulich, K. Gogoi, S.F. Dowdy, Enhancing endosomal escape for intracellular delivery of macromolecular biologic therapeutics, Sci. Rep. 6 (2016) 32301.
[32] S.L.Y. Teo, J.J. Rennick, D. Yuen, H. Al-Wassiti, A.P.R. Johnston, C.W. Pouton, Unravelling cytosolic delivery of cell penetrating peptides with a quantitative endosomal escape assay, Nat. Commun. 12 (2021) 3721.
[33] A.S. Dixon, M.K. Schwinn, M.P. Hall, K. Zimmerman, P. Otto, T.H. Lubben, B. L. Butler, B.F. Binkowski, T. Machleidt, T.A. Kirkland, M.G. Wood, C.T. Eggers, L. P. Encell, K.V. Wood, NanoLuc complementation reporter optimized for accurate measurement of protein interactions in cells, ACS Chem. Biol. 11 (2016) 400–408.
[34] M.A. Beach, S.L.Y. Teo, M.Z. Chen, S.A. Smith, C.W. Pouton, A.P.R. Johnston, G. K. Such, Quantifying the endosomal escape of pH-responsive nanoparticles using the split luciferase endosomal escape quantification assay, ACS Appl. Mater. Interfaces 14 (2022) 3653–3661.
[35] Y. Jiang, Q. Lu, Y. Wang, E. Xu, A. Ho, P. Singh, Y. Wang, Z. Jiang, F. Yang, G. T. Tietjen, P. Cresswell, W.M. Saltzman, Quantitating endosomal escape of a library of polymers for mRNA delivery, Nano Lett. 20 (2020) 1117–1123.
[36] Y. Rui, D.R. Wilson, S.Y. Tzeng, H.M. Yamagata, D. Sudhakar, M. Conge, C. A. Berlinicke, D.J. Zack, A. Tuesca, J.J. Green, High-throughput and high-content bioassay enables tuning of polyester nanoparticles for cellular uptake, endosomal escape, and systemic in vivo delivery of mRNA, Sci. Adv. 8 (2022) eabk2855.
[37] K.V. Kilchrist, S.C. Dimobi, M.A. Jackson, B.C. Evans, T.A. Werfel, E.A. Dailing, S. K. Bedingfield, I.B. Kelly, C.L. Duvall, Gal8 visualization of endosome disruption predicts carrier-mediated biologic drug intracellular bioavailability, ACS Nano 13 (2019) 1136–1152.
[38] A. Wittrup, A. Ai, X. Liu, P. Hamar, R. Trifonova, K. Charisse, M. Manoharan, T. Kirchhausen, J. Lieberman, Visualizing lipid-formulated siRNA release from endosomes and target gene knockdown, Nat. Biotechnol. 33 (2015) 870–876.
[39] R.O. Egberink, A.H. van Asbeck, M. Boswinkel, G. Muradjan, J. Dieker, R. Brock, Deciphering structural determinants distinguishing active from inactive cell-penetrating peptides for cytosolic mRNA delivery, Bioconjug. Chem. 34 (2023) 1822–1834.
[40] F. Distelmaier, H.J. Visch, J.A. Smeitink, E. Mayatepek, W.J. Koopman, P. H. Willems, The antioxidant Trolox restores mitochondrial membrane potential and Ca2+ -stimulated ATP production in human complex I deficiency, J. Mol. Med. 87 (2009) 515–522.
[41] J. Ma, J.J. van den Beucken, S.K. Both, H.J. Prins, M.N. Helder, F. Yang, J. A. Jansen, Osteogenic capacity of human BM-MSCs, AT-MSCs and their co-cultures using HUVECs in FBS and PL supplemented media, J. Tissue Eng. Regen. Med. 9 (2015) 779–788.
[42] M. Dominici, K. Le Blanc, I. Mueller, I. Slaper-Cortenbach, F. Marini, D. Krause, R. Deans, A. Keating, D. Prockop, E. Horwitz, Minimal criteria for defining multipotent mesenchymal stromal cells. The international society for cellular therapy position statement, Cytotherapy 8 (2006) 315–317.
[43] V. Palacio-Castaneda, R. Oude Egberink, A. Sait, L. Andree, B.M. Sala, N. Hassani Besheli, E. Oosterwijk, J. Nilvebrant, S.C.G. Leeuwenburgh, R. Brock, W.P. R. Verdurmen, Mimicking the biology of engineered protein and mRNA nanoparticle delivery using a versatile microfluidic platform, Pharmaceutics 13 (2021).
[44] R. Oude Egberink, H.M. Zegelaar, N. El Boujnouni, E.M.M. Versteeg, W.F. Daamen, R. Brock, Biomaterial-mediated protein expression induced by peptide-mRNA nanoparticles embedded in lyophilized collagen scaffolds, Pharmaceutics 14 (2022).
[45] R.A. McCloy, S. Rogers, C.E. Caldon, T. Lorca, A. Castro, A. Burgess, Partial inhibition of Cdk1 in G 2 phase overrides the SAC and decouples mitotic events, Cell Cycle 13 (2014) 1400–1412.
[46] S. Bolte, F.P. Cordelieres, A guided tour into subcellular colocalization analysis in light microscopy, J. Microsc. 224 (2006) 213–232.
[47] S.V. Costes, D. Daelemans, E.H. Cho, Z. Dobbin, G. Pavlakis, S. Lockett, Automatic and quantitative measurement of protein-protein colocalization in live cells, Biophys. J. 86 (2004) 3993–4003.
[48] L. Nahidiazar, A.V. Agronskaia, J. Broertjes, B. van den Broek, K. Jalink, Optimizing imaging conditions for demanding multi-color super resolution localization microscopy, PLoS One 11 (2016) e0158884.
[49] V. Neviani, S. van Deventer, T.P. Worner, K.T. Xenaki, M. van de Waterbeemd, R.N. P. Rodenburg, I.M.N. Wortel, J.K. Kuiper, S. Huisman, J. Granneman, P.M.P. van Bergen En, A.J.R. Henegouwen, A.B. van Heck, P.G. Spriel, Site-specific functionality and tryptophan mimicry of lipidation in tetraspanin CD9, FEBS J. 287 (2020) 5323–5344.
[50] M. Ovesny, P. Krizek, J. Borkovec, Z. Svindrych, G.M. Hagen, ThunderSTORM: a comprehensive ImageJ plug-in for PALM and STORM data analysis and super-resolution imaging, Bioinformatics 30 (2014) 2389–2390.
[51] I.M. Khater, I.R. Nabi, G. Hamarneh, A review of super-resolution single-molecule localization microscopy cluster analysis and quantification methods, Patterns (n y) 1 (2020) 100038.
[52] K. van den Dries, S.L. Schwartz, J. Byars, M.B. Meddens, M. Bolomini-Vittori, D. S. Lidke, C.G. Figdor, K.A. Lidke, A. Cambi, Dual-color superresolution microscopy reveals nanoscale organization of mechanosensory podosomes, Mol. Biol. Cell 24 (2013) 2112–2123.
[53] A.H. van Asbeck, A. Beyerle, H. McNeill, P.H. Bovee-Geurts, S. Lindberg, W. P. Verdurmen, M. Hallbrink, U. Langel, O. Heidenreich, R. Brock, Molecular parameters of siRNA-cell penetrating peptide nanocomplexes for efficient cellular delivery, ACS Nano 7 (2013) 3797–3807.
[54] M.L. van der Bent, O. Paulino da Silva Filho, M. Willemse, M. Hallbrink, D.G. Wansink, R. Brock, The nuclear concentration required for antisense oligonucleotide activity in myotonic dystrophy cells, FASEB J, (2019) fj201900263R.
[55] R.O. Egberink, A.H. van Asbeck, M. Boswinkel, G. Muradjan, J. Dieker, R. Brock, Deciphering structural determinants distinguishing active from inactive cell-penetrating peptides for cytosolic mRNA delivery, Bioconjug. Chem. (2023).
[56] S. El Andaloussi, P. Guterstam, U. Langel, Assessing the delivery efficacy and internalization route of cell-penetrating peptides, Nat. Protoc. 2 (2007) 2043–2047.
[57] F. Duchardt, M. Fotin-Mleczek, H. Schwarz, R. Fischer, R. Brock, A comprehensive model for the endocytic uptake of cationic cell-penetrating peptides, Traffic 8 (2007) 848–866.
[58] K.L. Veiman, I. Mager, K. Ezzat, H. Margus, T. Lehto, K. Langel, K. Kurrikoff, P. Arukuusk, J. Suhorutsenko, K. Padari, M. Pooga, T. Lehto, U. Langel, PepFect14 peptide vector for efficient gene delivery in cell cultures, Mol. Pharm. 10 (2013) 199–210.
[59] A.H. van Asbeck, J. Dieker, R. Oude Egberink, L. van den Berg, J. van der Vlag, R. Brock, Protein Expression Correlates Linearly with mRNA Dose over Up to Five Orders of Magnitude In Vitro and In Vivo, Biomedicines, 9 (2021).
[60] B. Neuhaus, B. Tosun, A. Rotan, A. Frede, M. Westendorf, M. Epple, Nanoparticles as transfection agents: a comprehensive study with ten different cell lines, RSC Adv. 6 (2016) 18102–18112.
[61] N. Feiner-Gracia, R.A. Olea, R. Fitzner, N. El Boujnouni, A.H. van Asbeck, R. Brock, L. Albertazzi, Super-resolution imaging of structure, molecular composition, and stability of single oligonucleotide polyplexes, Nano Lett. 19 (2019) 2784–2792.
[62] Q. Li, L. Zhang, J. Lang, Z. Tan, Q. Feng, F. Zhu, G. Liu, Z. Ying, X. Yu, H. Feng, H. Yi, Q. Wen, T. Jin, K. Cheng, X. Zhao, M. Ge, Lipid-peptide-mRNA nanoparticles augment radioiodine uptake in anaplastic thyroid cancer, Adv Sci (weinh) 10 (2023) e2204334.
[63] J. Yoo, D. Lee, V. Gujrati, N.S. Rejinold, K.M. Lekshmi, S. Uthaman, C. Jeong, I. K. Park, S. Jon, Y.C. Kim, Bioreducible branched poly(modified nona-arginine) cell-penetrating peptide as a novel gene delivery platform, J. Control. Release 246 (2017) 142–154.
[64] M. Mae, S. El Andaloussi, P. Lundin, N. Oskolkov, H.J. Johansson, P. Guterstam, U. Langel, A stearylated CPP for delivery of splice correcting oligonucleotides using a non-covalent co-incubation strategy, J. Control. Release 134 (2009) 221–227.
[65] H. Zhang, J. Bussmann, F.H. Huhnke, J. Devoldere, A.K. Minnaert, W. Jiskoot, F. Serwane, J. Spatz, M. Roding, S.C. De Smedt, K. Braeckmans, K. Remaut, Together is better: mRNA co-encapsulation in lipoplexes is required to obtain ratiometric co-delivery and protein expression on the single cell level, Adv Sci (weinh) 9 (2022) e2102072.
[66] M. Dowaidar, M. Gestin, C.P. Cerrato, M.H. Jafferali, H. Margus, P.A. Kivistik, K. Ezzat, E. Hallberg, M. Pooga, M. Hallbrink, U. Langel, Role of autophagy in cell-penetrating peptide transfection model, Sci. Rep. 7 (2017) 12635.
[67] M. de Beer, D. Daviran, R. Roverts, L. Rutten, E. Macias-Sanchez, J.R. Metz, N. Sommerdijk, A. Akiva, Precise targeting for 3D cryo-correlative light and electron microscopy volume imaging of tissues using a FinderTOP, Commun Biol 6 (2023) 510.
[68] A. David, B.P. Dolan, H.D. Hickman, J.J. Knowlton, G. Clavarino, P. Pierre, J. R. Bennink, J.W. Yewdell, Nuclear translation visualized by ribosome-bound nascent chain puromycylation, J. Cell Biol. 197 (2012) 45–57.
[69] A. Krhac Levacic, S. Berger, J. Muller, A. Wegner, U. Lachelt, C. Dohmen, C. Rudolph, E. Wagner, Dynamic mRNA polyplexes benefit from bioreducible cleavage sites for in vitro and in vivo transfer, J. Control. Release 339 (2021) 27–40.
[70] S. Ali, C. Dussouillez, B. Padilla, B. Frisch, A.J. Mason, A. Kichler, Design of a new cell penetrating peptide for DNA, siRNA and mRNA delivery, J. Gene Med. 24 (2022) e3401.
[71] Z. ur Rehman, D. Hoekstra, I.S. Zuhorn, Mechanism of polyplex- and lipoplex-mediated delivery of nucleic acids: real-time visualization of transient membrane destabilization without endosomal lysis, ACS Nano, 7 (2013) 3767-3777.
[72] M.G. Prieve, P. Harvie, S.D. Monahan, D. Roy, A.G. Li, T.L. Blevins, A.E. Paschal, M. Waldheim, E.C. Bell, A. Galperin, J.R. Ella-Menye, M.E. Houston, Targeted mRNA therapy for ornithine transcarbamylase deficiency, Mol. Ther. 26 (2018) 801–813.